

Full paper

Asperity shape in flexoelectric/triboelectric contacts

Karl P. Olson, Laurence D. Marks*

Northwestern University, Department of Materials Science and Engineering, 2220 Campus Drive, Room 2036, Evanston, IL 60208, United States



ARTICLE INFO

Keywords:

Triboelectricity
Flexoelectricity
Contact Mechanics
Electromechanics
Asperity Shape
Charge Transfer Scaling

ABSTRACT

Triboelectric and flexoelectric phenomena have seen significant recent interest for energy harvesting. However, the underlying science responsible for triboelectricity has yet to be completely understood, both the fundamentals and an understanding of how the energy output depends upon the shape of the interacting surface. Here, we investigate the role of the contacting shapes (asperities) in triboelectricity. We demonstrate that their shape and size is very important, obtaining qualitative agreement with experimental results. Further, we discuss how the impact of the shape depends on material, geometric, gradient elasticity and electronic transport details. We provide scaling rules which can be exploited to better design energy harvesting devices based upon either triboelectricity or flexoelectricity.

1. Introduction

Triboelectricity, the charge transfer between two contacting or rubbing materials, is of interest in a wide range of scientific, engineering, and everyday applications. In some, such as in the design of triboelectric nanogenerators (TENGs) [1,2] large charge transfer is desirable. In others, less charge transfer is preferable, e.g., to prevent industrial accidents [3], pharmaceutical powder clumping [4–6], or excessive charging of space exploration vehicles [7]. Triboelectricity is also important in diverse scientific areas, from planetary formation [8] to the effect of shampoos on the static electricity of human hair [9]. Despite an increasing interest in triboelectric research, many details of the mechanism and relevant materials and geometrical properties are still unknown [10–12].

Some aspects of triboelectricity are established, and there is an analogy to a capacitor and compensating charges [13,14]. If there is a potential difference between two materials due to the difference in their work functions (contact potential), this can be thought of as equivalent to the potential difference across a capacitor. The charge to compensate this will be that which cancels the electric field. It has been known for many decades [15] that if an insulating dielectric is in between the two materials, then this will lead to a polarization P , a bulk bound charge of $-\nabla \cdot P$ and a bound surface charge of $P \cdot \hat{n}$, where \hat{n} is the surface normal [16]. The total charge is then the combination of the bound surface charge from the polarization and that from the potential.

Previously, we have pointed out that triboelectricity occurs at contacting asperities, where electromechanical potentials large enough to

drive charge transfer form due to asperity deformation [17,18]. A significant contribution is due to the flexoelectric effect, the polarization caused by strain gradients, which should be combined with the contact potential between the two materials. Flexoelectric theory dates back to the 1960s [19,20], and it has become an increasingly popular research topic as the small length scales of nanotechnology lead to inherently large gradients. The field grew especially after the seminal measurements by Ma and Cross [21], and flexoelectric contributions have been shown to be important for a variety of electronic materials and devices [3], such as switching of ferroelectrics [22,23] or transistors [24] and photovoltaics [25], as well as a wider variety of fields including planetary formation [8] and bone healing [26]. Several reviews provide further background on flexoelectricity and its wider effects in electronic materials [27–30].

Evidence for the importance of flexoelectricity in triboelectricity can be traced back to the work of Jamieson in 1910 [31], who showed that bending a piece of cellulose changed the sign of the tribocharge. This was taken further in 1917 by Shaw [32] who explored more materials, demonstrating that some were more positive with positive curvature, while others were more negative, and similar work has continued to the modern day [33]. The work of Jamieson and Shaw predates the formal theory of flexoelectricity by about 50 years [19,20]. Recent work has continued to support the connection between triboelectricity and flexoelectricity [17,18,34–38],

Going beyond this, we have also developed a more detailed model to analyze the electromechanics of single-asperity contacts [39]. The contact of asperities is simplified to a spherical metal indenter that is

* Corresponding author.

E-mail addresses: karlolson@u.northwestern.edu (K.P. Olson), l-marks@northwestern.edu, laurence.marks@gmail.com (L.D. Marks).

pressed into a semi-infinite semiconductor slab. The deformation is determined using Hertzian contact solutions [40], and the electronic band bending is calculated by considering electromechanical and other relevant electronic effects.

One unresolved issue concerns the asperity shape, for which generalizations that can be used to assist design of energy harvesting devices are desirable. In tribology, the shape of asperities is in some cases considered to have little importance, such as its effect on real contact areas [41,42] or on friction [43]. In other cases, tribological quantities of interest, such as leakage from a hydrodynamic film [43], creep at asperities [44], or wear rate in abrasives [45], are strongly dependent on asperity shape.

With a focus on triboelectricity, asperity shape effects have been studied as surface modifications of TENGs [46,47]. Microscale patterns have been created on the surface of materials by molding polymers to solid templates [48,49] or selectively melting polymer surfaces with lasers [50,51]. These studies indicate that surface modifications such as gratings, arrays of protrusions or divots often increase charge transfer, enhancing TENG performance. One work compared surfaces with regular arrays of microscale domes and pyramids to flat surfaces [49]. TENG open-circuit voltage and short-circuit current were increased by ~50% for domes and ~500% for pyramids. These results were attributed to increases in contact area, but the domes and pyramids would only increase the contact area by ~40% and ~30%, respectively. The difference in the electromechanics from the different asperity shapes is a significant part of this disparity. Other works have examined the effect of different surface morphologies on the performance of TENGs [48,52,53]. We will return to this at the end of this manuscript after presenting directly relevant theory.

Here, we consider the effect of the asperity shape on triboelectric polarization, bound surface charge and electromechanical band bending generated at contacts. We demonstrate the size scaling, as well as scaling with force and material dependent terms. Our theory explains results of experiments with surface modified TENGs, for which surface area changes alone are not adequate, and provides a foundation for future rational design of improved energy harvesting devices.

2. Theory

First, we examine the effect of asperity shape on electromechanical potentials, i.e., its effects on electronic band bending due to strain, via the deformation potential [54] and the mean inner potential [55], and that due to strain gradients via flexoelectricity. Depending on the materials involved, specific problems necessarily include other potentials. For example, the Nb:SrTiO₃ – Pt_{0.8}Ir_{0.2} case [39] requires consideration of the depletion potential. For this work, these material system dependent potentials are left aside. Unless otherwise noted, the calculations presented here consider a rigid indenter contacting a SrTiO₃ half-space and focus on the response of the half-space; two contacting asperities can be simplified to this case by using an effective radius [56]. We choose SrTiO₃ because it is well-characterized, but the analysis follows for any non-metal. Because SrTiO₃ is cubic, we may ignore piezoelectricity. To simplify the analysis, the indenter is assumed to have dielectric properties of vacuum. (We will pose determining all the necessary parameters for other materials as a challenge to the community.) For further details regarding the calculations and relevant SrTiO₃ parameters, see [Supplementary Material SN1](#).

We consider the five asperity shape cases shown in [Fig. 1](#). The 3-D axisymmetric cases are sphere, cylinder, and cone indenters, shown in [Fig. 1a-c](#). The 2-D cases with axial symmetry correspond to indenters in the shape of an infinitely long cylinder or rectangular prism, shown in [Fig. 1d-e](#) and are referred to as a roller and punch, respectively. While real asperity shapes are intermediate to these, they provide bounds to what can be expected for more realistic shapes [45]. How the results scale is discussed in terms of the mean contact pressure and contact radius, which may be calculated for more complex asperity shapes.

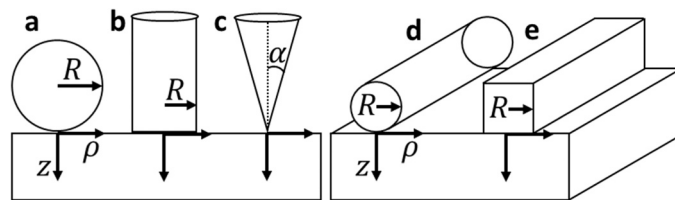


Fig. 1. Sketches, axis definitions, and geometric parameters for the five indenter cases: (a) sphere, (b) cylinder, (c) cone, (d) roller, and (e) punch.

The stress field in the elastic half-space is calculated from Hertz-like solutions [57–59] for a sphere of radius R , a cylinder of radius R , a cone with half-angle α measured from the vertical, a roller of radius R , and a punch of half-width R . These Hertzian solutions assume the pressure distribution at the surface, given in [Table 1](#), is limited to the region inside the contact radius, where p_m is the mean contact pressure, a the contact radius, F the force on the indenter in the 3-D cases or the force per unit length in the 2-D cases, and Y the Young's modulus of the half-space. The superscripts *s*, *cy*, *co*, *r*, and *p* refer to the sphere, cylinder, cone, roller, and punch, respectively. Note that none of these pressure distributions are differentiable at the edge of the contact region, $\rho = a$. While this is physically unreasonable, Hertzian solutions nonetheless give results with acceptable error for many contact problems [60]. In the cylinder, cone, and punch cases, the sharp corners cause unresolvable numerical singularities. For these cases, contact solutions that incorporate strain gradient elasticity [61,62] and eliminate this singularity are used with a length scale parameter of about $\ell = 0.04a$, corresponding to a contact radius of about 10 nm [63] (see [Supplementary Material SN3](#)). We also consider a third 2-D case, a triangular prism with half-angle α , in the scaling results. It is not included in further calculations because there is no strain gradient solution that would be needed for the sharp contact point. For discussion of an elastic spherical indenter, see [Supplementary Material SN2](#).

The results of specific cases are, of course, dependent on F , R or a , and Y , but two generalizations and reductions are possible:

1. The stress inside the half-space is proportional to p_m , so the strain is proportional to p_m/Y , strain gradient to p_m/aY , and polarization to $p_m\mu/aY$.
2. Normalizing the coordinates \mathbf{r} by the contact radius a results in a natural scaling.

Specifically, the stresses σ_{ij} , strains ϵ_{ij} , strain gradients $\partial\epsilon_{kl}/\partial x_j = \epsilon_{klj}$, and flexoelectric polarizations $P_i = \mu_{klij}\epsilon_{klj}$ scale as shown in [Table 1](#), where μ_{klij} is a flexoelectric tensor component.

Since SrTiO₃ is cubic, there are three independent flexoelectric components, namely $\mu_{iii} = -36.9\text{nC/m}$, $\mu_{ijj} = -40.2\text{nC/m}$, and $\mu_{ijj} = -1.4\text{nC/m}$, which are referred to as the longitudinal, transverse, and shear components, respectively [64]. We note that, like dielectric constants, flexoelectric tensor components are normally quoted in the zero-frequency limit. Since flexoelectric polarization is connected to the dielectric behavior, there can be significant changes such as near phase transitions [65,66]. There can also be large frequency dependencies of the flexoelectric coefficients and hence the polarization for some materials [67]. In the analysis herein, we consider only the zero-frequency limit.

[Table 1](#) includes only the parameters that lead to simple scaling. For example, each stress component depends differently on Poisson's ratio [57–59], so these quantities vary in a complex manner. We will now focus our attention on the scaling of the electromechanical potential Φ_{EM} , which is obtained by determining the charge density and solving Poisson's equation.

In the strained half-space, flexoelectricity produces a polarization density due to the strain gradient. The potential due to a polarization

Table 1

Contact mechanics parameters and scaling for the six indenter shapes. $\sigma_z(z=0)$ is the surface stress profile, a the contact radius, $p_m = F/a^2$ the mean contact pressure, and σ_{ij} , ε_{ij} , and P_i the stress, strain, and polarization in the half space, respectively. Note that $\sigma_{ij}(\frac{\mathbf{r}}{a}) \propto p_m$, $\varepsilon_{ij}(\frac{\mathbf{r}}{a}) \propto p_m/Y$, and $P_i(\frac{\mathbf{r}}{a}) \propto \mu_{klj} \varepsilon_{klj}(\frac{\mathbf{r}}{a}) \propto p_m \mu / aY$.

Asperity Shape	$\frac{\sigma_z(z=0)}{p_m}$	a	$\sigma_{ij}(\frac{\mathbf{r}}{a}) \propto$	$\varepsilon_{ij}(\frac{\mathbf{r}}{a}) \propto$	$P_i(\frac{\mathbf{r}}{a}) \propto$
Sphere (s)	$\frac{3}{2} \left(1 - \frac{\nu^2}{a^2}\right)^{\frac{1}{2}}$	$\left(\frac{3(1-\nu^2)RF}{4Y}\right)^{\frac{1}{2}}$	$\left(\frac{FY^2}{R^2}\right)^{\frac{1}{2}}$	$\left(\frac{F}{R^2Y}\right)^{\frac{1}{2}}$	$\frac{\mu}{R}$
Cylinder (cy)	$\frac{1}{2} \left(1 - \frac{\nu^2}{a^2}\right)^{\frac{1}{2}}$	R	$\frac{F}{R^2}$	$\frac{F}{R^2Y}$	$\frac{F\mu}{R^3Y}$
Cone (co)	$\cosh^{-1} \frac{a}{\rho}$	$\left(2(1-\nu^2) \frac{F \tan \alpha}{Y}\right)^{\frac{1}{2}}$	$\frac{Y}{\tan \alpha}$	$\frac{1}{\tan \alpha}$	$\left(\frac{Y}{F \tan^3 \alpha}\right)^{\frac{1}{2}} \mu$
Roller (r)	$\frac{4}{\pi} \left(1 - \frac{\nu^2}{a^2}\right)^{\frac{1}{2}}$	$\left(\frac{4(1-\nu^2)FR}{\pi Y}\right)^{\frac{1}{2}}$	$\left(\frac{FY}{R}\right)^{\frac{1}{2}}$	$\left(\frac{F}{RY}\right)^{\frac{1}{2}}$	$\frac{\mu}{R}$
Punch (p)	$\frac{2}{\pi} \left(1 - \frac{\nu^2}{a^2}\right)^{\frac{1}{2}}$	R	$\frac{F}{R}$	$\frac{F}{RY}$	$\frac{F\mu}{R^2Y}$
Triangular Prism	$\frac{2}{\pi} \cosh^{-1} \frac{a}{x}$	$\frac{(1-\nu^2)F \tan \alpha}{2Y}$	$\frac{Y}{\tan \alpha}$	$\frac{1}{\tan \alpha}$	$\frac{Y\mu}{F \tan^2 \alpha}$

density $P(\mathbf{r})$ can be determined by considering the equivalent potential produced by the bulk and surface bound charge densities,

$$q^{\text{FXE}}(\mathbf{r}) = -\nabla \cdot P(\mathbf{r}); \zeta^{\text{FXE}}(\mathbf{r}) = P(\mathbf{r}) \cdot \hat{n} \quad (1)$$

respectively, where \hat{n} is a unit vector normal to the surface. Far away from the contact in the vacuum or deep into the material, the two cancel so the potential decays faster than that of a simple charge; near the surface the surface bound charge density dominates.

The volumetric strain ε_{vol} has two effects on the potential. First, the average potential in the crystal, or mean inner potential (MIP), shifts with strain [55]. For SrTiO₃, this shift is given by $\varphi = \frac{\partial \text{MIP}}{\partial \varepsilon_{\text{vol}}} = 22.2 \text{ eV}$. Also, since we are interested in charge transfer, we examine the behavior of the conduction band energy E_C . This shifts relative to the MIP by an amount $D_{\text{BS}}^C = \frac{\partial(E_C - \text{MIP})}{\partial \varepsilon_{\text{vol}}} = -17.2 \text{ eV}$, known as the conduction-band-specific deformation potential [54]. The valence band could be treated similarly using the valence-band-specific deformation potential instead. Like the flexoelectric polarization, the potential due to the volumetric strain, $(D_{\text{BS}}^C + \varphi)\varepsilon_{\text{vol}}(\mathbf{r})$, has a corresponding charge density, $\varphi^{\text{MIP,DP}}(\mathbf{r}) = -\nabla \cdot (\varepsilon(\mathbf{r}) \nabla [(D_{\text{BS}}^C + \varphi)\varepsilon_{\text{vol}}])$, determined by solving Poisson's equation where $\varepsilon(\mathbf{r})$ is the (in general, spatially-varying) dielectric permittivity. Then, the electromechanical potential $\Phi^{\text{EM}}(\mathbf{r})$, which includes the flexoelectric, mean inner potential, and conduction-band specific deformation potential is given by the solution to

$$-\nabla \cdot (\varepsilon(\mathbf{r}) \nabla \Phi^{\text{EM}}(\mathbf{r})) = \varphi^{\text{EM}}(\mathbf{r}) = \varphi^{\text{MIP,DP}}(\mathbf{r}) + q^{\text{FXE}}(\mathbf{r}) + \zeta^{\text{FXE}}(\mathbf{r}) \quad (2)$$

where $\varphi^{\text{EM}}(\mathbf{r})$ is the total bound charge density due to electromechanical effects. Finally, we note that in both the solution for $\varphi^{\text{MIP,DP}}$ and of Eq. (2), we include the image charges and dielectric screening created by the surface of the half-space [68].

In Eq. (2), if the bulk flexoelectric term q^{FXE} dominates, then $\varphi^{\text{EM}} \propto \nabla \cdot P \propto p_m / a^2 Y$. If the surface term ζ^{FXE} dominates instead, then $\varphi^{\text{EM}} \propto P \cdot \hat{n} \propto p_m / aY$. Finally, if the strain-dependent term $\varphi^{\text{MIP,DP}}$ dominates, $\varphi^{\text{EM}} \propto \nabla^2 \varepsilon_{\text{vol}} \propto p_m / a^2 Y$. Ignoring any variation in the dielectric permittivity that may occur due to mechanical effects, $\nabla^2 \Phi^{\text{EM}} \propto \varphi^{\text{EM}} / \varepsilon$, so the potential will scale as $\Phi^{\text{EM}} \propto p_m / Y$ if either bulk term, q^{FXE} or $\varphi^{\text{MIP,DP}}$, dominates, or as $\Phi^{\text{EM}} \propto a p_m / Y$ if the surface term ζ^{FXE} dominates. In our calculations with SrTiO₃, we find $\Phi^{\text{EM}} \propto p_m / Y$.

3. Results

3.1. Potentials, charges densities, and electromechanical energies

Figs. 2 and 3 show $\Phi_{\text{EM}}/(p_m/Y)$ and $\varphi_{\text{EM}}/(p_m/a^2Y)$ plotted against normalized coordinates \mathbf{r}/a for the five indenter shapes. In the 3-D cases (a-c), the cylinder case is clearly distinct, while the sphere and cone share many features. This is caused by the surface stress distribution being most concentrated at the edge of contact in the case of the cylinder, while it is most concentrated at the center in the sphere and cone cases. This leads to the sphere and cone sharing a similar surface charge density (see Figs S1-S5c). When the effect of the sharp corner of the cone is reduced by strain gradient solutions, the sphere and the cone solutions approach each other closer, further supporting this reasoning (see Figs S1 and S3). The 2-D cases follow intuition; the roller is most similar to the sphere, and the punch to the cylinder. Despite the similarities in Figs. 2 and 3 for various indenter shapes, the scaling remains vastly different in accordance with Table 1.

Understanding the energies involved in electromechanical contacts can give further insight into the problem. A simplified thermodynamic potential density Ψ , ignoring piezoelectric terms and terms with more than one polarization gradient, gives the following form [28].

$$\Psi = -\frac{1}{2} \sigma_{ij} \varepsilon_{ij} - \frac{f_{ijkl}}{2} \left(P_k(\mathbf{r}) \frac{\partial \varepsilon_{ij}(\mathbf{r})}{\partial x_l} - \varepsilon_{ij}(\mathbf{r}) \frac{\partial P_k(\mathbf{r})}{\partial x_l} \right) - \frac{1}{2} \epsilon_{ij}^{-1} P_i(\mathbf{r}) P_j(\mathbf{r}) \quad (3)$$

The strain energy density is $E'_{\text{strain}}(\mathbf{r}) = \sigma_{ij}(\mathbf{r}) \varepsilon_{ij}(\mathbf{r}) / 2$. The stress and strain are proportional to p_m and p_m / Y , respectively when plotted against the normalized axes \mathbf{r}/a . Therefore, the total strain energy integrated over the whole half-space volume Ω is $E_{\text{strain}} = \int_{\Omega} E'_{\text{strain}}(\mathbf{r}) d\mathbf{r} \propto a^3 p_m^2 / Y$. For example, the total strain energy for spherical contacts is $E_{\text{strain}}^s \propto (F^5 / RY^2)^{\frac{1}{3}}$, and, from the calculations, $E_{\text{strain}}^s / \left(\frac{F^5}{RY^2} \right)^{\frac{1}{3}} = 2.6$.

The flexoelectric energy density is $E'_{\text{FXE}}(\mathbf{r}) = \frac{f_{ijkl}}{2} \left(P_k(\mathbf{r}) \frac{\partial \varepsilon_{ij}(\mathbf{r})}{\partial x_l} - \varepsilon_{ij}(\mathbf{r}) \frac{\partial P_k(\mathbf{r})}{\partial x_l} \right)$ where f is the flexocoupling tensor defined by $\mu_{ijkl} = \epsilon_{hk} f_{ijkl}$. The strain and polarization are proportional to p_m / Y and $p_m \mu / aY$, respectively, so the total flexoelectric energy is $E_{\text{FXE}} = \int_{\Omega} E'_{\text{FXE}}(\mathbf{r}) d\mathbf{r} \propto a p_m^2 \mu^2 / Y^2$. For spherical contacts, $E_{\text{FXE}}^s \propto F \mu^2 / RY$, and $E_{\text{FXE}}^s /$

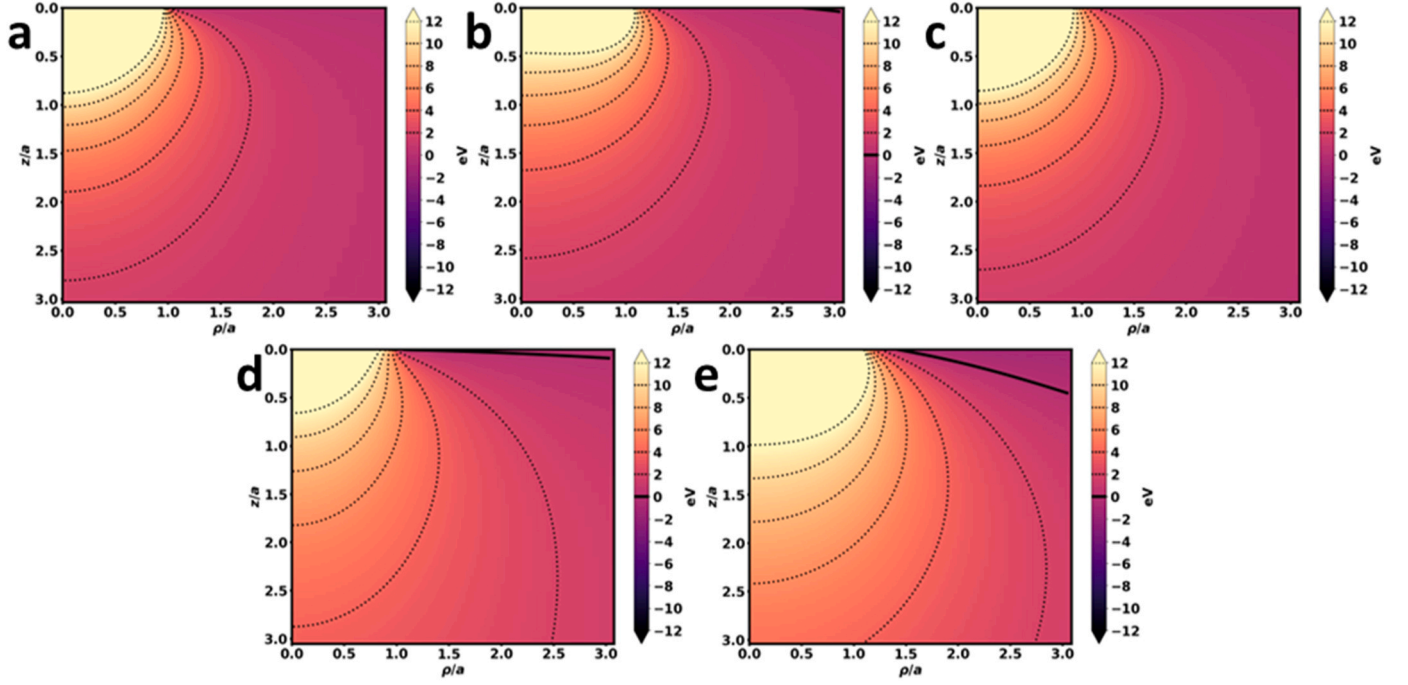


Fig. 2. Plots of $\Phi_{EM}/(p_m/Y)$ for different indenter shapes: (a) sphere, (b) cylinder (c) cone, (d) roller, and (e) punch. The ρ and z axes are normalized by the contact radius a . Contour lines are labeled in the color bar.

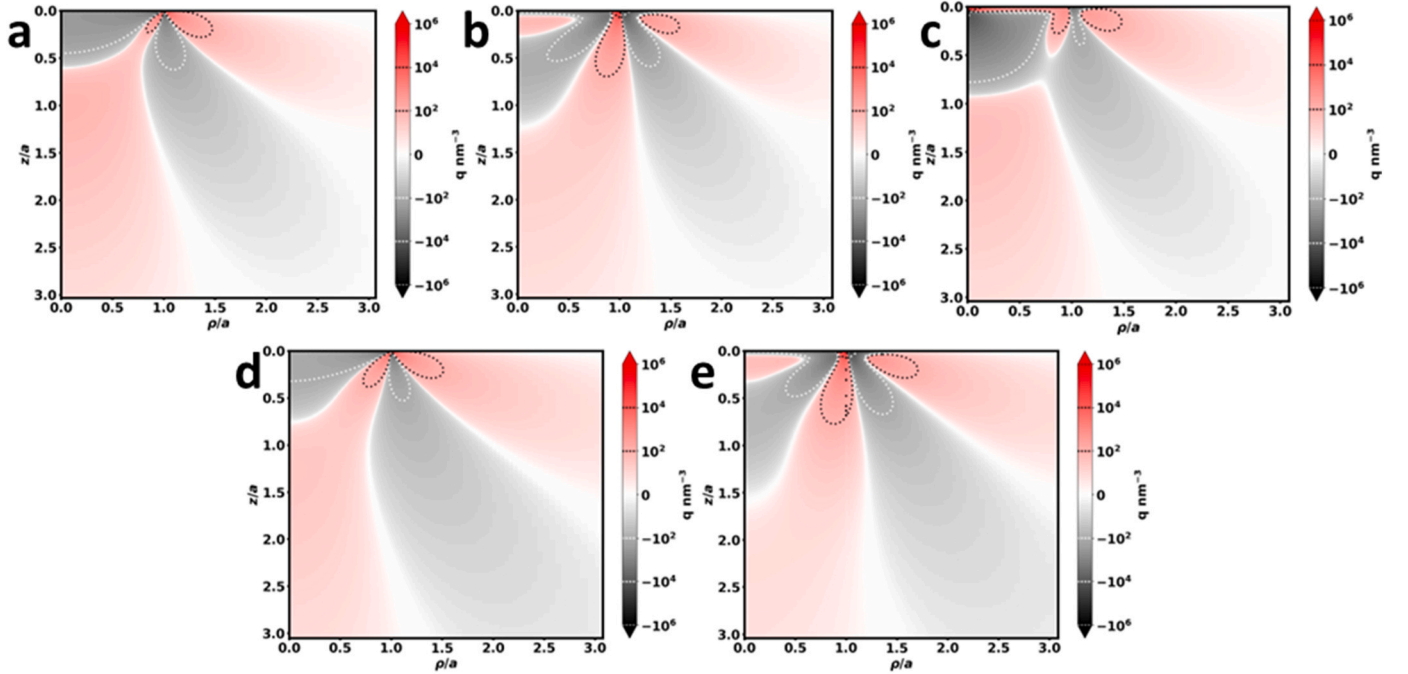


Fig. 3. Plots of $\mathcal{E}_{EM}/(p_m/a^2Y)$ for different indenter shapes: (a) sphere, (b) cylinder (c) cone, (d) roller, and (e) punch. The ρ and z axes are normalized by the contact radius a . Contour lines are labeled in the color bar.

$\left(\frac{F\mu^2}{RY}\right) = 3.1\text{m/nF}$, where we have used $\mu = \mu_{ijij}$, the flexoelectric tensor component with the largest magnitude.

Finally, the polarization energy density is $E_p(\mathbf{r}) = \epsilon_{ij}^{-1}P_i(\mathbf{r})P_j(\mathbf{r})/2$. The polarization is proportional to $p_m\mu/aY$, so the total polarization energy is $E_p = \int_{\Omega} E_p(\mathbf{r}) d\mathbf{r} \propto p_m^2\mu^2/Y^2$. For spherical contacts, $E_p \propto F\mu^2/R$, and $E_p/\left(\frac{F\mu^2}{RY}\right) = 1.7\text{m/nF}$. Note that this scales in the same manner as

E_{FXE} , which should be expected because the only source of polarization we consider is the flexoelectric effect. Plots of the energy densities and other results are found in [Supplementary Material S5](#) and [Figs. S8-S10](#).

Compared to the strain energy, the scaling of the flexoelectric and polarization energies shows that the flexoelectric effect becomes more important when the contact radius and modulus become smaller. This follows the intuition that when gradients become large at small scales, especially the nanoscale, flexoelectricity becomes increasingly

important.

3.2. Contribution of flexoelectric tensor components

A less material-specific analysis can be realized by considering Φ^{EM} when $\mu_{ijkl} = 0$ or when $D_{\text{BS}}^{\text{C}} + \varphi = 0$, i.e., when the electromechanical response is due to only the deformation potential and mean inner potential shift or only flexoelectricity. We define

$$-\nabla \cdot (\epsilon(\mathbf{r}) \nabla \Phi^{\text{MIP,DP}}(\mathbf{r})) = \varphi^{\text{MIP,DP}}(\mathbf{r}) \quad (4)$$

$$-\nabla \cdot (\epsilon(\mathbf{r}) \nabla \Phi^{\text{FXE}}(\mathbf{r})) = \varrho^{\text{FXE}}(\mathbf{r}) = \varrho^{\text{FXE}}(\mathbf{r}) + \zeta^{\text{FXE}}(\mathbf{r}) \quad (5)$$

where $\Phi^{\text{MIP,DP}}$ and Φ^{FXE} correspond to these two cases, respectively. Further, we consider three separate components of Φ^{FXE} that each depend on only one of the three independent flexoelectric coefficients in a cubic system. That is, we set all but one flexoelectric coefficient to zero and calculate Φ^{FXE} . These results are more applicable to materials other than SrTiO_3 ; they remain dependent on the mechanical and dielectric properties of SrTiO_3 , but not on other electronic properties, notably including the flexoelectric coefficients. Components of the bound charges can be calculated similarly (see [Supplementary Material SN4](#)). For a sphere indenter, the result is plotted in [Fig. 4](#), which has three cases: non-zero longitudinal ($\mu_{iii} \neq 0$), non-zero transverse ($\mu_{ijj} \neq 0$), and non-zero shear ($\mu_{ijj} \neq 0$) flexoelectric coefficients. Φ^{EM} can be obtained by simply adding in the appropriate proportions the Φ^{FXE} terms and $(D_{\text{BS}}^{\text{C}} + \varphi) \epsilon_{\text{vol}}(F, \mathbf{r})$, as shown in [Eq. \(6\)](#).

$$\Phi_{\text{EM}} = \mu_{iii} \Phi_{\text{longitudinal}}^{\text{FXE}} + \mu_{ijj} \Phi_{\text{transverse}}^{\text{FXE}} + \mu_{ijj} \Phi_{\text{shear}}^{\text{FXE}} + (D_{\text{BS}}^{\text{C}} + \varphi) \epsilon_{\text{vol}} \quad (6)$$

[Fig. 4a-c](#) and [S6a-c](#) show that the flexoelectric component contributions to the potential have differing shapes and magnitudes, while the bound charge contributions have similar shapes but with the

longitudinal component contributing an opposite sign to the transverse and shear. For a normalized flexoelectric coefficient, the longitudinal and transverse components contribute similar magnitudes, while the shear contributes much more. However, as is true for SrTiO_3 , the shear flexoelectric component is often much smaller than the others [\[64\]](#).

[Fig. S7a-c](#) shows that the transverse flexoelectric component is largely dominant in determining the flexoelectric surface charge, except close to the contact edge ($\rho \approx a$), where the shear component becomes relevant.

4. Discussion

We have calculated normalized electromechanical potentials and bound charge densities for a variety of rigid indenter shapes contacting an elastic half-space and described how the potentials and thermodynamic elastic, flexoelectric, and polarization energies scale with indenter force and size, as well as slab modulus. The shape of asperities is important in triboelectricity because it affects how Φ_{EM} scales, as well as the shape of the potentials and charge densities, as shown in [Figs. 2 and 3](#).

[Fig. 4, S6 and S7](#) emphasize that the ratios between components of a material's flexoelectric tensor control the shapes of the potential and charge densities. For cases unlike SrTiO_3 , the shapes may change dramatically (though the scaling remains the same). Therefore, determining the relative magnitudes of the flexoelectric coefficients for materials of interest is helpful in informing the design of triboelectric devices using those materials.

We can quantitatively match experimental scalings for triboelectric experiments that have been performed with different asperity shapes and/or different roughness. Consider surface-modified polydimethylsiloxane (PDMS) films of [Varghese et al. \[49\]](#). We estimate the increase in contact area using the reported measurements and the

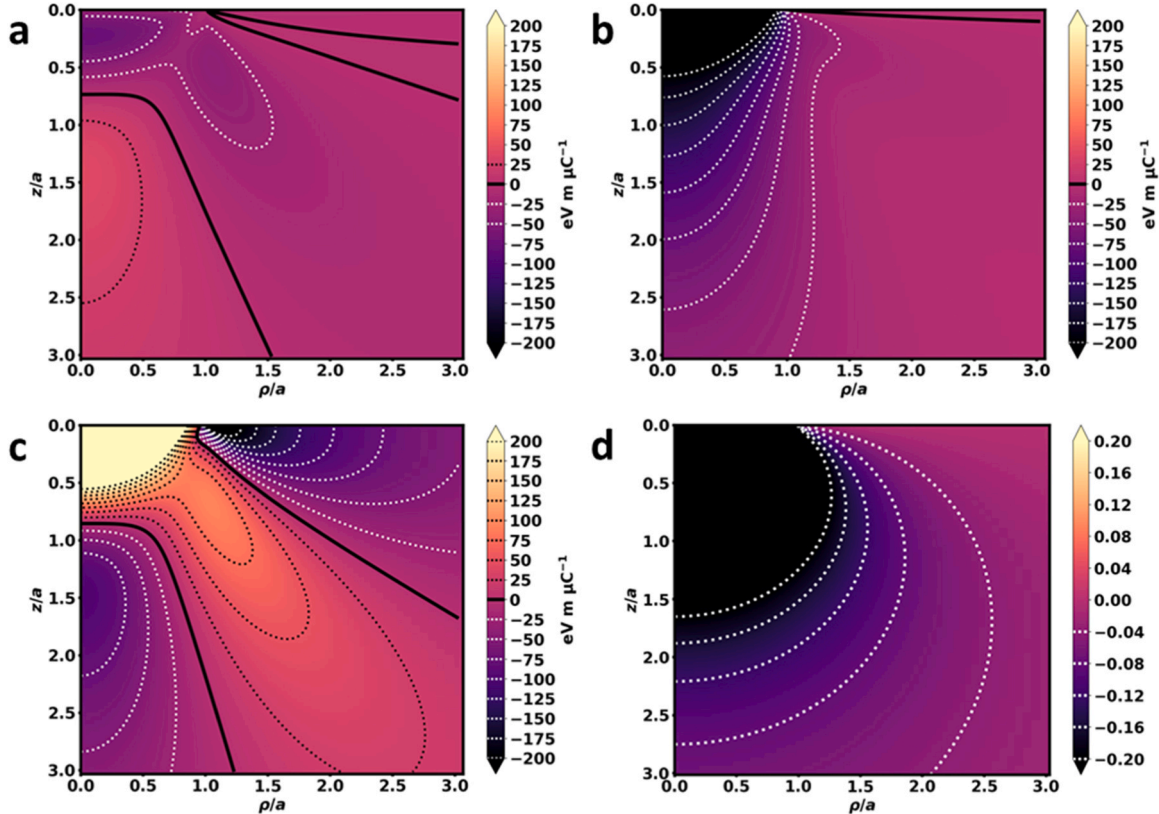


Fig. 4. Plots of (a-c) $\Phi_{\text{EM}}/(D_m/\mu'Y)$ with artificial flexoelectric coefficients and (d) $\epsilon_{\text{vol}}/(D_m/Y)$ for a rigid sphere indenter.: (a) $\mu_{iii} = \mu', \mu_{ijj} = \mu_{ijj} = 0$. (b) $\mu_{ijj} = \mu', \mu_{iii} = \mu_{ijj} = 0$. (c) $\mu_{ijj} = \mu', \mu_{iii} = \mu_{ijj} = 0$.

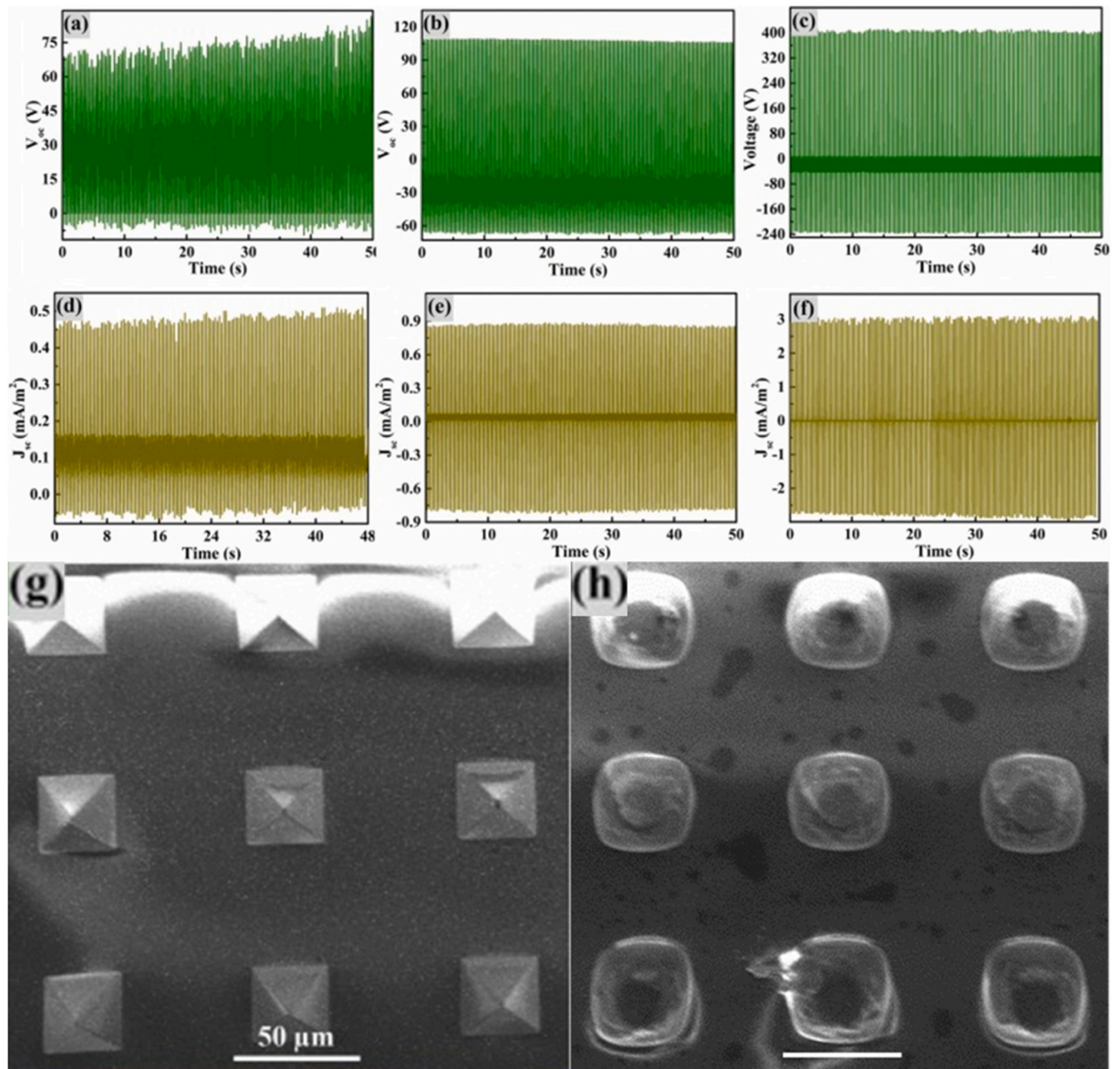


Fig. 5. Experimental data of micro-patterned TENGs from Varghese, et al.: (a-c, d-f) Open-circuit voltage and short-circuit current, respectively, measured for a cellulose acetate nanofiber/micro-patterned PDMS TENG, with (a,d) flat, (b,e) dome, and (c,f) pyramid micropatterns. (g,h) SEM images of (g) pyramid and (h) dome micropatterns. The scalebar in both images is 50 μm . Reprinted from Nano Energy, 98, Varghese, H., H. M. A. Hakkeem, K. Chauhan, E. Thouti, S. Pillai and A. Chandran, A high-performance flexible triboelectric nanogenerator based on cellulose acetate nanofibers and micropatterned PDMS films as mechanical energy harvester and self-powered vibrational sensor, 107339, Copyright (2022), with permission from Elsevier.

images reproduced in Fig. 5g-h. We assume that the domes are half-spheres, that the height of the pyramids is equal to their side length, and that the cellulose acetate nanofiber can be modeled as homogenous, since the fiber size is much smaller than the domes and pyramids. Then there is approximately a 40% and 30% increase in surface area for domes and pyramids, respectively. However, they observe an increase in short-circuit current density of about 70% for domes and 500% for pyramids, as well as an open-circuit voltage increase of about 40% for domes, and 430% for pyramids.

We map the pyramids to cones with half angle of 45° and use spheres for the domes with radius given by Varghese, 21 μm . Then, if the 3 N

force is spread evenly over the artificial asperities, which have number density $\sim 150 \text{ mm}^{-2}$ across the 2 cm^2 sample, and we take the modulus [69] of the Sylgard 184 PDMS to be 1.32 MPa, we can calculate the polarization energies E_p for the two asperity shapes. For the pyramids,

$$E_p = 2.0 \text{ m/nF} \left(\frac{F}{Y \tan^3 \alpha} \right)^{\frac{1}{2}} \mu^2 = 18 \text{ kNm}^3 \text{ C}^{-2} \mu^2 \text{ and for the domes,}$$

$$E_{\text{FXE}} = 1.7 \text{ m/nF} \frac{F}{RY} \mu^2 = 6.2 \text{ kNm}^3 \text{ C}^{-2} \mu^2. \text{ These have a ratio of 2.9, and the polarization energies similarly have a ratio of 3.0. These are compared to the relative difference between the experimental open-circuit voltages and closed-circuit current densities, which have ratios of about 3.8 and 3.5, respectively, in excellent agreement. Further}$$

details and additional explanations of other experimental results can be found in [Supplementary Material SN6](#).

5. Conclusion

In conclusion, without the addition of any empirical parameters, using analytical models of elasticity and the consequent flexoelectric polarization, we have demonstrated significant dependence upon asperity shape which agrees with experimental results. Furthermore, we have provided scaling relationships so these results can be applied generally to assist in optimizing flexoelectric and triboelectric energy harvesting strategies. We pose as a challenge to the community measuring key materials properties such as flexoelectric coefficients and deformation potentials when comparing triboelectric performance. This work also contributes to the increasing evidence that flexoelectricity plays a major role in triboelectricity, as first suggested by the experiments of Jamieson [31] and Shaw [32] over a century ago and well before there was any theory for strain-gradient polarization.

Funding sources

This work was supported by Northwestern University McCormick School of Engineering.

Notes

The complete copyright license for [Fig. 5](#) may be found online at <https://s100.copyright.com/CustomerAdmin/PLF.jsp?ref=6445462d-c5dc-4ec7-acdc-362821236051>.

CRediT authorship contribution statement

Karl P. Olson: Methodology, Software, Validation, Formal analysis, Investigation, Data curation, Writing – original draft, Visualization. **Laurence D. Marks:** Conceptualization, Methodology, Formal analysis, Resources, Writing – review & editing, Supervision, Project administration, Funding acquisition.

Declaration of Competing Interest

The authors declare that they have no known competing financial interests or personal relationships that could have appeared to influence the work reported in this paper.

Data Availability

Data will be made available upon reasonable request to the corresponding author.

Appendix A. Supporting information

Supplementary data associated with this article can be found in the online version at [doi:10.1016/j.nanoen.2023.109036](https://doi.org/10.1016/j.nanoen.2023.109036).

References

- F.-R. Fan, Z.-Q. Tian, Z. Lin Wang, Flexible triboelectric generator, *Nano Energy* 1 (2012) 328–334, <https://doi.org/10.1016/j.nanoen.2012.01.004>.
- W.-G. Kim, D.-W. Kim, I.-W. Tcho, J.-K. Kim, M.-S. Kim, Y.-K. Choi, Triboelectric nanogenerator: structure, mechanism, and applications, *ACS Nano* 15 (2021) 258–287, <https://doi.org/10.1021/acsnano.0c09803>.
- S.-C. Liang, J.-P. Zhang, L.-S. Fan, Electrostatic characteristics of hydrated lime powder during transport, *Ind. Eng. Chem. Res.* 35 (1996) 2748–2755, <https://doi.org/10.1021/ie9506678>.
- H. Watanabe, M. Ghadiri, T. Matsuyama, Y.L. Ding, K.G. Pitt, H. Maruyama, et al., Triboelectrification of pharmaceutical powders by particle impact, *Int. J. Pharm.* 334 (2007) 149–155, <https://doi.org/10.1016/j.ijpharm.2006.11.005>.
- J. Wong, P.C.L. Kwok, H.-K. Chan, Electrostatics in pharmaceutical solids, *Chem. Eng. Sci.* 125 (2015) 225–237, <https://doi.org/10.1016/j.ces.2014.05.037>.
- S. Naik, B. Hancock, Y. Abramov, W. Yu, M. Rowland, Z. Huang, et al., Quantification of tribocharging of pharmaceutical powders in V-blenders: experiments, multiscale modeling, and simulations, *J. Pharm. Sci.* 105 (2016) 1467–1477, <https://doi.org/10.1016/j.xphs.2015.12.024>.
- S.K. Mishra, T. Sana, Mitigating massive triboelectric charging of drill in shadowed region of Moon, *Mon. Not. R. Astron. Soc.* 512 (2022) 4730–4735, <https://doi.org/10.1093/mnras/stac369>.
- T. Steinpilz, K. Joeris, F. Jungmann, D. Wolf, L. Brendel, J. Teiser, et al., Electrical charging overcomes the bouncing barrier in planet formation, *Nat. Phys.* 16 (2019) 225–229, <https://doi.org/10.1038/s41567-019-0728-9>.
- C.M. Mills, V.C. Ester, H. Henkin, Measurement of static charge on hair, *J. Soc. Cosmet. Chem.* 7 (1956) 466–475, <https://library.sconline.org/v007n05/51>.
- M.W. Williams, Triboelectric charging of insulating polymers—some new perspectives, *AIP Adv.* 2 (2012), 010701, <https://doi.org/10.1063/1.3687233>.
- S.H. Pan, Z.N. Zhang, Fundamental theories and basic principles of triboelectric effect: a review, *Friction* 7 (2019) 2–17, <https://doi.org/10.1007/s40544-018-0217-7>.
- D.J. Lacks, T. Shinbrot, Long-standing and unresolved issues in triboelectric charging, *Nat. Rev. Chem.* 3 (2019) 465–476, <https://doi.org/10.1038/s41570-019-0115-1>.
- S. Matsusaka, H. Maruyama, T. Matsuyama, M. Ghadiri, Triboelectric charging of powders: a review, *Chem. Eng. Sci.* 65 (2010) 5781–5807, <https://doi.org/10.1016/j.ces.2010.07.005>.
- L. Xie, J. Li, Y. Liu, Review on charging model of sand particles due to collisions, *Theor. Appl. Mech. Lett.* 10 (2020) 276–285, <https://doi.org/10.1016/j.taml.2020.01.047>.
- L.H. Fisher, On the representation of the static polarization of rigid dielectrics by equivalent charge distributions, *Am. J. Phys.* 19 (1951) 73–78, <https://doi.org/10.1119/1.1932714>.
- D. Griffiths, *Electric fields in matter*, in: J. Smith (Ed.), *Introduction to Electrodynamics*, 4 ed., Pearson Education, Inc., 2013, pp. 167–209.
- C.A. Mizzi, A.Y.W. Lin, L.D. Marks, Does flexoelectricity drive triboelectricity? *Phys. Rev. Lett.* 123 (2019), 116103 <https://doi.org/10.1103/PhysRevLett.123.116103>.
- C.A. Mizzi, L.D. Marks, When flexoelectricity drives triboelectricity, *Nano Lett.* 22 (2022) 3939–3945, <https://doi.org/10.1021/acsnanolett.2c00240>.
- S.M. Kogan, Piezoelectric effect during inhomogeneous deformation and acoustic scattering of carriers in crystals, *Sov. Phys. - Sol. State* 5 (1964) 2069–2070.
- E.V. Bursian, O.I. Zaikovskii, Changes in the curvature of a ferroelectric film due to polarization, *Soviet Phys. - Solid State* 10 (1968) 1121–1124.
- W.H. Ma, L.E. Cross, Observation of the flexoelectric effect in relaxor Pb(Mg_{1/3}Nb_{2/3})O₃ ceramics, *Appl. Phys. Lett.* 78 (2001) 2920–2921, <https://doi.org/10.1063/1.1356444>.
- H. Lu, C.W. Bark, D. Esque De Los Ojos, J. Alcalá, C.B. Eom, G. Catalan, et al., Mechanical writing of ferroelectric polarization, *Science* 335 (2012) 59–61, <https://doi.org/10.1126/science.1218693>.
- J. Ocenasek, H. Lu, C.W. Bark, C.B. Eom, J. Alcalá, G. Catalan, et al., Nanomechanics of flexoelectric switching, *Phys. Rev. B* 92 (2015), <https://doi.org/10.1103/PhysRevB.92.035417>.
- D. Guo, P. Guo, L. Ren, Y. Yao, W. Wang, M. Jia, et al., Silicon flexoelectronic transistors, *Sci. Adv.* 9 (2023), eadd3310, <https://doi.org/10.1126/sciadv.add3310>.
- M.-M. Yang, D.J. Kim, M. Alexe, Flexo-photovoltaic effect, *Science* 360 (2018) 904–907, <https://doi.org/10.1126/science.aan3256>.
- F. Vazquez-Sancho, A. Abdollahi, D. Damjanovic, G. Catalan, Flexoelectricity in bones, *Adv. Mater.* 30 (2018), <https://doi.org/10.1002/adma.201705316>.
- P. Zubko, G. Catalan, A.K. Tagantsev, Flexoelectric effect in solids, *Nann. Rev. Mater. Res.* 43 (2013) 387–421, <https://doi.org/10.1146/annurev-matsci-071312-121634>.
- P.V. Yudin, A.K. Tagantsev, Fundamentals of flexoelectricity in solids, *Nanotechnology* 24 (2013), 432001, <https://doi.org/10.1088/0957-4484/24/43/432001>.
- Z.L. Wang, Y. Zhang, W. Hu, Flexoelectric effect, in: Z.L. Wang, Y. Zhang, W. Hu (Eds.), *Piezotronics and Piezo-Phototronics: Applications to Third-Generation Semiconductors*, Springer Nature Switzerland, Cham, 2023, pp. 529–550.
- R.A. Surmeneva, M.A. Surmeneva, The influence of the flexoelectric effect on materials properties with the emphasis on photovoltaic and related applications: a review, *Mater. Today* 67 (2023) 256–298, <https://doi.org/10.1016/j.matod.2023.05.026>.
- W. Jamieson, The electrification of insulating materials, *Nature* 83 (1910) 189, <https://doi.org/10.1038/083189a0>.
- P.E. Shaw, Experiments on tribo-electricity. I. The tribo-electric series, *Proc. R. Soc. Lond. Ser. A-Contain. Pap. A Math. Phys. Character* 94 (1917) 16–33, <https://doi.org/10.1098/rspa.1917.0046>.
- R.K. Pandey, C.K. Ao, W. Lim, Y. Sun, X. Di, H. Nakanishi, et al., The relationship between static charge and shape, *ACS Cent. Sci.* 6 (2020) 704–714, <https://doi.org/10.1021/acscentsci.9b01108>.
- B.N.J. Persson, On the role of flexoelectricity in triboelectricity for randomly rough surfaces, *EPL (Europhys. Lett.)* 129 (2020), <https://doi.org/10.1209/0295-5075/129/10006>.
- M. Kumar, J. Lim, J.-Y. Park, H. Seo, Flexoelectric effect driven colossal triboelectricity with multilayer graphene, *Curr. Appl. Phys.* 32 (2021) 59–65, <https://doi.org/10.1016/j.cap.2021.09.014>.
- H. Qiao, P. Zhao, O. Kwon, A. Sohn, F. Zhuo, D.-M. Lee, et al., Mixed triboelectric and flexoelectric charge transfer at the nanoscale, *Adv. Sci.* 8 (2021), 2101793, <https://doi.org/10.1002/advs.202101793>.

- [37] S. Lin, M. Zheng, L. Xu, L. Zhu, Z.L. Wang, Electron transfer driven by tip-induced flexoelectricity in contact electrification, *J. Phys. D: Appl. Phys.* 55 (2022), 315502, <https://doi.org/10.1088/1361-6463/ac6f2e>.
- [38] X. Lyu, M. MacGregor, J. Liu, N. Darwish, S. Ciampi, Direct-current output of silicon-organic monolayer-platinum Schottky TENGs: elusive friction-output relationship, *Nano Energy* 114 (2023), 108627, <https://doi.org/10.1016/j.nanoen.2023.108627>.
- [39] K.P. Olson, C.A. Mizzi, L.D. Marks, Band bending and ratcheting explain triboelectricity in a flexoelectric contact diode, *Nano Lett.* 22 (2022) 3914–3921, <https://doi.org/10.1021/acs.nanolett.2c00107>.
- [40] H. Hertz, Ueber die Berührung fester elastischer Körper, *J. Reine Angew. Math.* 1882 (1882) 156–171, <https://doi.org/10.1515/crll.1882.92.156>.
- [41] J.A. Greenwood, J.B.P. Williamson, F.P. Bowden, Contact of nominally flat surfaces, *Proc. R. Soc. Lond. A Math. Phys. Sci.* 295 (1966) 300–319, <https://doi.org/10.1098/rspa.1966.0242>.
- [42] B. Bhushan, Contact mechanics of rough surfaces in tribology: multiple asperity contact, *Tribol. Lett.* 4 (1998) 1–35, <https://doi.org/10.1023/A:1019186601445>.
- [43] R.B. Siripuram, L.S. Stephens, Effect of deterministic asperity geometry on hydrodynamic lubrication, *J. Tribol.* 126 (2004) 527–534, <https://doi.org/10.1115/1.1715104>.
- [44] F.J. Alamos, M. Philo, D.B. Go, S.R. Schmid, Asperity contact under creep conditions, *Tribol. Int.* 160 (2021), 107039, <https://doi.org/10.1016/j.triboint.2021.107039>.
- [45] D.V. De Pellegrin, G.W. Stachowiak, Evaluating the role of particle distribution and shape in two-body abrasion by statistical simulation, *Tribol. Int.* 37 (2004) 255–270, <https://doi.org/10.1016/j.triboint.2003.09.004>.
- [46] Y. Zou, J. Xu, K. Chen, J. Chen, Advances in nanostructures for high-performance triboelectric nanogenerators, *Adv. Mater. Technol.* 6 (2021), 2000916, <https://doi.org/10.1002/admt.202000916>.
- [47] I. Aazem, R. Walden, A. Babu, S.C. Pillai, Surface patterning strategies for performance enhancement in triboelectric nanogenerators, *Results Eng.* 16 (2022), 100756, <https://doi.org/10.1016/j.rineng.2022.100756>.
- [48] X.-W. Zhang, G.-Z. Li, G.-G. Wang, J.-L. Tian, Y.-L. Liu, D.-M. Ye, et al., High-performance triboelectric nanogenerator with double-surface shape-complementary microstructures prepared by using simple sandpaper templates, *ACS Sustain. Chem. Eng.* 6 (2018) 2283–2291, <https://doi.org/10.1021/acssuschemeng.7b03745>.
- [49] H. Varghese, H.M.A. Hakkeem, K. Chauhan, E. Thouti, S. Pillai, A. Chandran, A high-performance flexible triboelectric nanogenerator based on cellulose acetate nanofibers and micropatterned PDMS films as mechanical energy harvester and self-powered vibrational sensor, *Nano Energy* 98 (2022), 107339, <https://doi.org/10.1016/j.nanoen.2022.107339>.
- [50] J. Huang, X. Fu, G. Liu, S. Xu, X. Li, C. Zhang, et al., Micro/nano-structures-enhanced triboelectric nanogenerators by femtosecond laser direct writing, *Nano Energy* 62 (2019) 638–644, <https://doi.org/10.1016/j.nanoen.2019.05.081>.
- [51] M. Muthu, R. Pandey, X. Wang, A. Chandrasekhar, I.A. Palani, V. Singh, Enhancement of triboelectric nanogenerator output performance by laser 3D-surface pattern method for energy harvesting application, *Nano Energy* 78 (2020), 105205, <https://doi.org/10.1016/j.nanoen.2020.105205>.
- [52] M.A.P. Mahmud, J. Lee, G. Kim, H. Lim, K.-B. Choi, Improving the surface charge density of a contact-separation-based triboelectric nanogenerator by modifying the surface morphology, *Micro Eng.* 159 (2016) 102–107, <https://doi.org/10.1016/j.mee.2016.02.066>.
- [53] I.W. Tcho, W.G. Kim, S.B. Jeon, S.J. Park, B.J. Lee, H.K. Bae, et al., Surface structural analysis of a friction layer for a triboelectric nanogenerator, *Nano Energy* 42 (2017) 34–42, <https://doi.org/10.1016/j.nanoen.2017.10.037>.
- [54] M. Stengel, From flexoelectricity to absolute deformation potentials: the case of SrTiO₃, *Phys. Rev. B* 92 (2015), 205115, <https://doi.org/10.1103/PhysRevB.92.205115>.
- [55] C.A. Mizzi, L.D. Marks, The role of surfaces in flexoelectricity, *J. Appl. Phys.* 129 (2021), 224102, <https://doi.org/10.1063/5.0048920>.
- [56] Q.J. Wang, D. Zhu, Hertz theory: contact of spherical surfaces, in: Q.J. Wang, Y.-W. Chung (Eds.), *Encyclopedia of Tribology*, Springer US, Boston, MA, 2013, pp. 1654–1662.
- [57] E. M'Ewen, XLI, Stresses in elastic cylinders in contact along a generatrix (including the effect of tangential friction), *Philos. Mag.* 40 (1949) 454–459, <https://doi.org/10.1080/14786444908521733>.
- [58] K.L. Johnson, *Contact Mechanics*, Cambridge University Press, Cambridge, 1985.
- [59] A.C. Fischer-Cripps, Elastic indentation stress fields, in: F.F. Ling (Ed.), *Introduction to Contact Mechanics*, 2 ed., Springer US, New York, 2007, pp. 77–100.
- [60] K.L. Johnson, One hundred years of hertz contact, *Proc. Inst. Mech. Eng.* 196 (1982) 363–378, https://doi.org/10.1243/PIME_PROC_1982_196_039_02.
- [61] X. Gao, New Solutions of Half-Space Contact Problems using Potential Theory, Surface Elasticity and Strain Gradient Elasticity. Texas A&M University Theses, Dissertations, and Records of Study (2002–): Texas A&M University, 2011.
- [62] X.-L. Gao, S.-S. Zhou, Strain gradient solutions of half-space and half-plane contact problems, *Z. Angew. Math. Phys.* 64 (2013) 1363–1386, <https://doi.org/10.1007/s00033-012-0273-1>.
- [63] M. Stengel, Unified ab initio formulation of flexoelectricity and strain-gradient elasticity, *Phys. Rev. B* 93 (2016), 245107, <https://doi.org/10.1103/PhysRevB.93.245107>.
- [64] J.W. Hong, D. Vanderbilt, First-principles theory and calculation of flexoelectricity, *Phys. Rev. B* 88 (2013), 174107, <https://doi.org/10.1103/PhysRevB.88.174107>.
- [65] W.H. Ma, L.E. Cross, Flexoelectricity of barium titanate, *Appl. Phys. Lett.* 88 (2006), 232902, <https://doi.org/10.1063/1.2211309>.
- [66] X. Ke, Z. Hong, Q. Ma, X. Wen, Z. Wang, S. Yang, et al., Giant flexoelectric coefficients at critical ferroelectric transition, *Acta Mater.* 245 (2023), 118640, <https://doi.org/10.1016/j.actamat.2022.118640>.
- [67] L.L. Shu, M.Q. Wan, X.N. Jiang, F. Li, N.G. Zhou, W.B. Huang, et al., Frequency dispersion of flexoelectricity in PMN-PT single crystal, *AIP Adv.* 7 (2017), <https://doi.org/10.1063/1.4973684>.
- [68] C. Hogan, M. Palumbo, R. Del Sole, Theory of dielectric screening and electron energy loss spectroscopy at surfaces, *Cr Phys.* 10 (2009) 560–574, <https://doi.org/10.1016/j.cry.2009.03.015>.
- [69] R. Moučka, M. Sedláčik, J. Osicka, V. Pata, Mechanical properties of bulk Sylgard 184 and its extension with silicone oil, *Sci. Rep.* 11 (2021), 19090, <https://doi.org/10.1038/s41598-021-98694-2>.



Karl P. Olson received his bachelor's degree in materials science and engineering from the University of Minnesota – Twin Cities in 2019. He is now a Ph.D. candidate in the Department of Materials Science and Engineering at Northwestern University. His current research focuses on the fundamental mechanisms behind triboelectricity and the connection to flexoelectricity.



Laurence D. Marks is a Professor Emeritus at Northwestern University. He works in many areas ranging from triboelectricity and flexoelectricity to nanotribology, corrosion, nanoparticles, oxide surfaces and density functional theory fixed-point algorithms.